

Measurements of plankton distribution in the ocean using submersible holography

Edwin Malkiel, Omar Alquaddoomi and Joseph Katz

Department of Mechanical Engineering, The Johns Hopkins University, Baltimore, MD 21218, USA

Received 5 October 1999, in final form and accepted for publication 19 October 1999

Abstract. A submersible holography system for *in situ* recordings of the spatial distribution of plankton has been developed and deployed. The system utilizes a ruby laser with an in-line recording configuration and has a sample volume of 732 ml. The reconstructed images have a resolution ranging from 10–20 μm for spherical particles and 3 μm for linear particles that lie within 100 mm from the film. Reconstructed volumes from holograms recorded during two recent deployments in the Strait of Georgia are scanned to obtain focused images of the particles, their position, size and orientation. The particles are also classified to several groups based on their morphological characteristics. The holograms include a set recorded during a 15 min vertical transect of the top 30 m of the water column. Along with the holograms, the data include records of depth, temperature, salinity, dissolved oxygen and optical transmissivity. The results show substantial variations in population makeup between layers spaced a short distance apart, particle concentration maxima at and near a pycnocline and evidence of zooplankton migration. A predominant horizontal diatom orientation is indicated in the region of peak diatom concentration. Individual holograms show clustering within different classes of plankton.

Keywords: holography, plankton distribution, thin layer, copepod

1. Introduction

As demand on the world's fisheries increases, there is considerable concern over the sustainability of such resources. There is also concern over the increasing frequency of harmful algal blooms in coastal waters, not only because of their effect on the fisheries, but also because of their effect on people. In order to introduce effective regulations to maintain our resources, we need a better understanding of the marine ecosystem in general and relevant plankton population dynamics in particular.

Population dynamics are governed by growth and mortality rates of phytoplankton and zooplankton. Obviously, the character of the environment, especially the predator–prey distribution, influences these rates. There is increasing evidence that small-scale turbulence also plays an important role; an entire volume of the *Scientia Marina* (Marrase *et al* 1997) has been dedicated to it. For example, turbulence can enhance phytoplankton growth by increasing nutrient diffusion (Karp-Boss *et al* 1996) or damage structures through shear, which increases their mortality. A step higher in the food web, turbulence can increase the feeding rates of zooplankton (Rothschild and Osborn 1988) or interfere with their ability to capture food (Svendsen 1997, Kiorboe 1997). These conclusions and hypotheses are based either on theoretical reasoning and laboratory data or on inference, based on

sampling of plankton (or chemical indicators for their abundance), on nutrient distributions, and on point measurements and turbulence statistics. *In situ* simultaneous measurement of turbulence and particle distributions are critical for relating laboratory data (e.g. on the effect of shear stress on plankton species) and the actual conditions in the field (i.e. the effect of turbulence on algal blooms). Turbulence dissipation rates averaged over scales of metres, that have been reported in the literature, do not determine the local shear stresses at the scale and location of the plankton.

Holography is ideally suited for studying the microstructure of this environment. In general, optical imaging at the proper magnification allows one to classify individual particles, determine individual locations and orientations, while acoustic methods cannot. Double exposures can show how these particles move in time. Non-motile and sufficiently small particles which follow the flow can be used as 'passive tracers' for measuring the velocity field. The advantage of holography over digital or video imaging, which has had considerable success (e.g. Gallager 1996, Tiselius 1998), is its ability to resolve small particles over a considerably larger sample volume. A planar imaging system which can resolve 20 μm can do so over a depth of field, D , equal to d^2/λ , where d is the resolution and λ is the wavelength of the light. For $\lambda = 694 \text{ nm}$ (the wavelength in our present system), and $d = 20 \mu\text{m}$, the depth of field is 0.6 mm. In comparison,

a hologram providing similar resolution can have a depth of field over a 100 times larger and, unlike a scanning planar system, it can record it instantaneously, which is a necessity for three-dimensional velocity measurements.

Implementation of holography for plankton detection started during the late 1960s and early 1970s, initially in laboratory studies (Knox 1966, Knox and Brooks 1969, Stewart *et al* 1973, Heflinger *et al* 1973). Carder (1979) measured the sizes, shapes and settling speeds of microscopic particles by recording sequential transmission holograms in the laboratory. Later, Carder *et al* (1982) developed a submersible holographic particle velocimeter for *in situ* measurement of sizes and settling rates of oceanic particulates within a free-floating sediment trap. However, being limited by laser power (they used a 2 mW, CW He-Ne laser) the sample volume was only a few mm³ and a typical hologram contained 30 particles. Katz *et al* (1984) and O'Hern *et al* (1988) developed the first submersible, pulsed-laser-based holography system and used it to measure the particle and bubble distributions in waters off Catalina Island, CA. More recently, Watson *et al* (1995), Foster and Watson (1997) and Hobson *et al* (1997) used hologrammetry to study the distribution of plankton in observation tanks.

A more recent pulsed-laser submersible system that can be used for recording *in situ* holograms of plankton is introduced in Katz *et al* (1999) and described briefly in section 2 of this paper. It records single or multiple-exposure holograms of a sample volume with size ranging from 732–1964 cm³. When reconstructed they provide information on the particles' sizes, shapes, orientations and positions in space. Ultimately, doubly exposed holograms recorded by this system can be analysed to provide the distributions of plankton and velocity (i.e. structure of the turbulence) simultaneously. Techniques to compute the three-dimensional velocity fields from laboratory, doubly exposed holograms of fluids seeded with microscopic particles have already been established (Barnhart *et al* 1994, Meng and Hussain 1995, Zhang *et al* 1997, Tao *et al* 1999, Meng 1999). Measured plankton distributions along with their environment, obtained in two deployments of the submersible holocamera, are presented in section 3. The measurements demonstrate the substantial variation of populations between layers, clustering, particle concentration maxima at and near a pycnocline as well as evidence of zooplankton migration.

2. The submersible holocamera and analysis procedures

2.1. Submersible system

We have opted for in-line holography because of its simplicity and suitability for far-field measurements of small particles. As figure 1 shows, laser output is spatially filtered and collimated to produce a uniform beam 76 mm in diameter. This beam passes horizontally through the ambient water between two windows and illuminates the particles situated within the path of the beam. The light diffracted by the particles interferes with the remaining undisturbed beam and the interference pattern is recorded on high-resolution

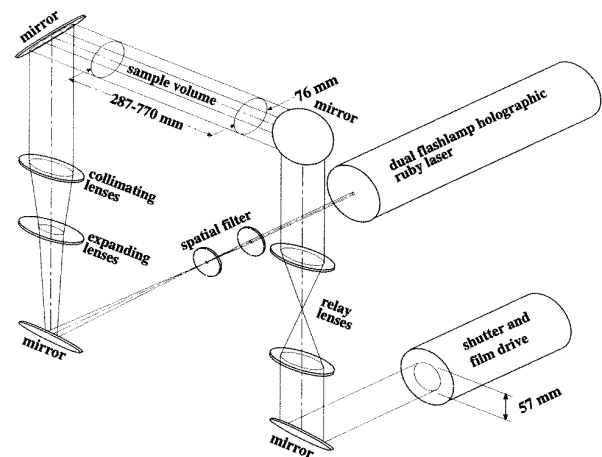


Figure 1. Holocamera optical setup for in-line holography.

film. Since an effort is made to keep the sample volume a substantial distance away from the bulk of the holocamera, relay lenses are inserted in the optical path in order to bring the image of the particles close to the film plane. By decreasing the particle-to-film distance, resolution improves, as it is dependent on the amplitude of the recorded interference pattern (Collier *et al* 1971). The aperture of the film drive shutter (presently 57 mm) and the adjustable separation distance between the camera and the laser delimit the size of the sample volume. We have mostly operated with a configuration that allows recording of a 287 mm long sample, yielding a 732 cm³ volume. Within this volume a hologram recorded during a field test contains between 5000 to 20 000 identifiable particles, which is relative sparse compared with its capability. Laboratory tests using a sample volume of 50 × 50 × 50 mm³ containing particles in the 10–100 μm range have shown that it is still possible to obtain clear images when the concentration is 1000 particles ml⁻¹, i.e. ~100 000 particles per in-line hologram. At higher concentrations, the image deteriorates. The concentration of particles in laboratory off-axis holograms can be more than an order of magnitude higher (Zhang *et al* 1997).

The light source for the submersible holocamera is a Q-switched, high-coherence ruby laser, which delivers 30 mJ of 694.3 nm light during a 30 ns pulse. The laser is custom built with two sets of flashlamps and is equipped with four Pockel's cell drivers. With these features, each time it is fired (up to three times per minute), it produces either one or two internal flashes (delays > 1 ms), with one or two laser pulses per flash (delays 10–1300 μs). On the receiving end, the film drive is equipped to record double exposures on the same frame or single exposures in sequence via a fast frame advance mode (10 ms). This feature is useful for velocity measurements. All the optical mounts of the laser have been rebuilt with rugged supports to enable operation in the field. For reliable operation, it is also critical to maintain the laser at a stable temperature (presently, 15 °C). This is accomplished by connecting the laser to a temperature control system that includes a water reservoir, a circulating pump and a thermoelectric heating/cooling system that exchanges heat with the ocean. This system is effective in ocean temperatures ranging 0–30 °C. The power source for the whole system,

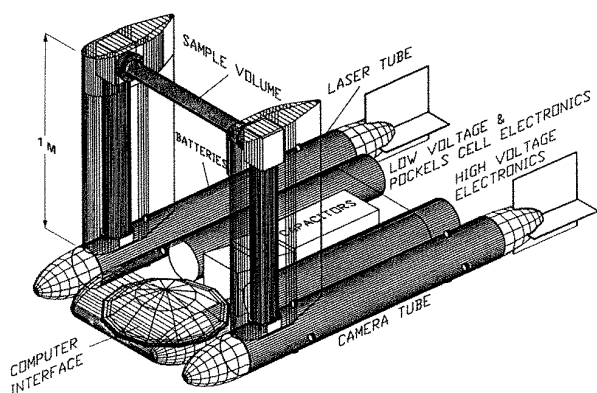


Figure 2. Basic external configuration of the holocamera.

two onboard batteries, provides sufficient energy to expose an entire roll of film (~300 holograms).

The external configuration of the submersible holographic camera is shown in figure 2. The electronics (much of which had been modified to fit) and optics are installed inside one dome-shaped chamber and four horizontal cylinders surrounding a compartment for batteries and capacitors. Prior to operation, all the cylinders can be purged and filled with N_2 to prevent condensation on the optics and electronics. All the cylinders also contain leak detectors at both ends. The laser cylinder and its attached vertical tube contain the laser and collimating optics. The camera cylinder and its vertical tube contain the receiving optics and film drive. The vertical tubes separate the sample volume from the horizontal cylinders by 89 cm and thus minimize its disturbance. Likewise, the vertical tubes are enshrouded in fairings (constructed of balsa wood to provide a high centre of buoyancy) and all the chambers are streamlined. Vertical fins/stabilizers located in the back keep the holocamera aligned with the mean flow (when it exists) to ensure that the sample volume is not located within the wake of any component. These steps are taken to reduce disturbances to the flow and minimize the possibility of triggering avoidance responses from zooplankton. Illuminating with red light is also useful in reducing the zooplankton response while recording multiple exposure holograms, which may be particularly significant when using directed light in the 460–530 nm range (Forward 1988, Buskey *et al* 1989).

This paper presents results from two deployments. In deployment A, the holocamera was equipped with a pair of flotation pontoons to make it a neutrally buoyant drifter. A remotely controlled ballast system was available for positioning the system at desirable depths (although we also recorded holograms while being suspended from the ship). A Sea Bird, Sea Cat CTD (conductivity, depth and salinity sensor) was installed within the fairing of the camera tube. It sampled water pumped from a port located near the sample volume. In deployment B, the holocamera was equipped with a towing harness and suspended from a crane at full weight (600 kg in air and 200 kg in water with the harness). The crane operator positioned the system at a desirable depth and the ship was allowed to drift. During this trip we also added a dissolved oxygen sensor and an optical transmissometer to the CTD package. Consequently, the instruments did not fit

within the fairing and we had to mount them externally with the intake port at nearly the same level as the sample volume, but 1.5 m behind it.

An operator communicates with the holocamera via two fibre optic lines. One line is used for controlling the system and transmitting CTD data (and signals from leak detectors) to a portable PC, which is used for operating and monitoring the system. The second fibre presently monitors the laser output but, since it is connected to an internal multiplexer, it can also transmit signals of up to three video cameras. These cables are currently only 130 m long, but can easily be extended. The maximum operational depth of the holocamera, prescribed by the glass windows, is 500 m. Further details on the system can be found in Katz *et al* (1999).

2.2. Film development and reconstruction

We currently use 70 mm AGFA 10E75 holography film, which is no longer manufactured, relying on accumulated stock until a suitable replacement is found. To insert or remove the film, the film drive needs to be removed from its cylinder. Exposed film is developed with a Kodak D-19 developer for 4 min at 20 °C so that the film attains an optical density of about 1.2. We get 'reconstructable' holograms by keeping the exposure levels in the 3–6 $\mu J cm^{-2}$ range, with the best contrast between images and background noise from midrange exposure levels.

The holograms are reconstructed using the setup illustrated in figure 3. A collimated and spatially filtered He–Ne laser beam (632.8 nm) illuminates the film, which recreates a three-dimensional image of the original sample volume. We view the hologram using a video camera equipped with a microscope lens (~2 times magnification on the CCD array, i.e. an entire video screen covers an area of $2.3 \times 1.7 mm^2$). The depth of field is less than 0.1 mm. This camera is mounted on a precision, three-axis translation stage, driven by stepper motors to provide precise coordinate information on the location of a displayed image in the reconstructed volume. Positioning and image grabbing are coordinated through a desktop computer. The net contraction of the reconstructed volume in the depth direction, due to reconstructing in air rather than water and using a different wavelength for illumination, is taken into account when determining the actual positions of objects. The contraction ratio is

$$\frac{Z_c}{Z} = \frac{\lambda n_c}{\lambda_c n}$$

where Z is the axial (depth) coordinate (normal to the surface of the hologram), λ is the recording wavelength (694 nm) and n is the refractive index of the sample volume (1.33), while Z_c , n_c (1.00) and λ_c (633 nm) are the respective quantities during reconstruction.

2.3. Species distribution

Sample images of the commonly encountered plankton from the holograms recorded in Georgia Strait (mostly from deployment B), are shown in figure 4. As the resolution in a

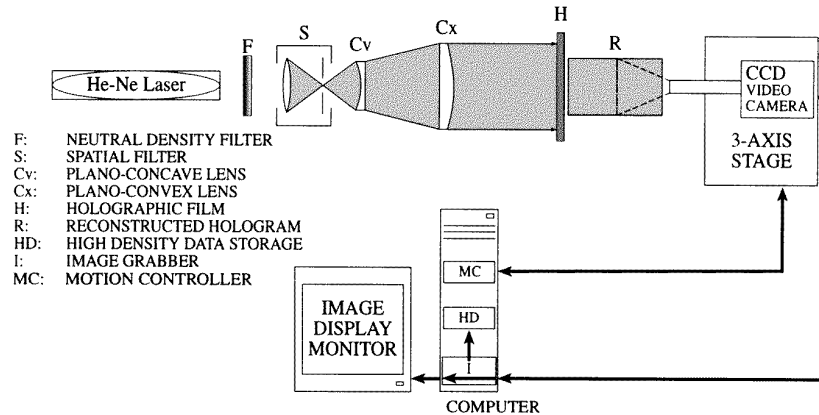


Figure 3. Setup for hologram reconstruction analysis.

holographic image is poorer than that obtained with an optical microscope used on physical samples, our classification scheme is based on gross morphological characteristics and size. For the purpose of comparison, benchmarking and species identification, during 'deployment A' we also siphoned water samples from the same depth while recording the holograms. The samples were examined under an optical microscope *in situ* (some were preserved and stored for further analysis). The species identification has been made by Jan Rines (private communication, see Katz *et al* (1999) for more details).

2.4. Resolution

The smallest individual particles that can be unambiguously distinguished from background speckle noise and measured, for at least the first 100 mm of the reconstructed volume, are in the 10–20 μm diameter range. The resolution for long, thin objects, such as the links between diatom frustules (figure 4(g)) or a flagellum on a dinoflagellate (figure 4(c)) is much better. For example, the setae (spines) in the species *Chaetoceros concavicornis* (or *convolutus*) shown in figure 4(f) have a thickness of less than 3 μm (samples of setae were measured under the microscope during deployment A–J Rines, private communication). However, our resolution is not sufficient for measuring the size of the setae directly from the reconstructed image. The object has to be larger than 10 μm before we can infer its size from its image. At greater depths the image quality deteriorates slightly. For example, at the far end of the sample volume, 220 mm from the film plane, Katz *et al* (1999) show that it is still possible to identify individual cells clearly but the 3 μm links between diatoms are no longer detectable.

Our resolution is reasonably good compared with the expected resolution (d_s) using an empirical relation (Vikram 1992) for in-line holograms made with uniform, collimated illumination:

$$d_s = \sqrt{\frac{Z\lambda}{100}}.$$

For spherical objects at a distance of 100 mm from the film plane the expected resolution is 25 μm at best. The capability of holograms to resolve linear structures smaller than the resolvable limit for spherical objects is well known (Vikram

1992). The difference occurs because a linear object, with the same diameter and distance away from the film plane as a spherical one, leaves an interference pattern of much higher amplitude. Consequently, it has a wider lateral extent on the hologram. The limit on resolution depends on the size of the 'aperture' of a particle, which is defined as the region on the film where the interference pattern is stronger than background noise. Using the amplitude at the centre of the pattern as a measure of detectability, the resolution, d_l , of an infinitely long linear object is

$$\frac{d_l}{d_s} = \frac{\pi}{4} \frac{1}{\sqrt{Z\lambda/d_s^2}}.$$

For a case with $d_s = 20 \mu\text{m}$, $Z = 100 \text{ mm}$, d_l would have to be only 1.2 μm to be detected, i.e. d_l is only a fraction of the diameter of the spherical object. In spite of the fact that the axial extents of the linear particles in our holograms are much smaller than Z , the diameter down to which they are detectable is consistent with this result.

2.5. Analysis

We currently make interactive, computer assisted scans of the reconstructed volume to obtain particle information. A computer program guides the camera through sections of reconstructed volume, and allows the user to stop and fine tune the camera position when an object comes into focus. At this point, the user selects and records a region that includes the focused particle image, measures its length and orientation and classifies it according to its shape and size. Subsequently, this image, the centroid location, size, shape and classification are stored automatically to a database. By selectively recording images, we substantially reduce the total image data per hologram (~85 GB), which could amount from recording images every 0.5 mm in depth at 4 $\mu\text{m}/\text{pixel}$ magnification, without image compression. As the holograms contain 5000–20 000 resolvable particles (figure 8), with the average particle image requiring less than 50 Kb, the selective recording reduces the total space required per hologram to the range of 250–1000 MB. Although we have semi-automated the scanning, measurement and classification processes, it still takes anywhere from 100–400 h to scan a single hologram depending on particle

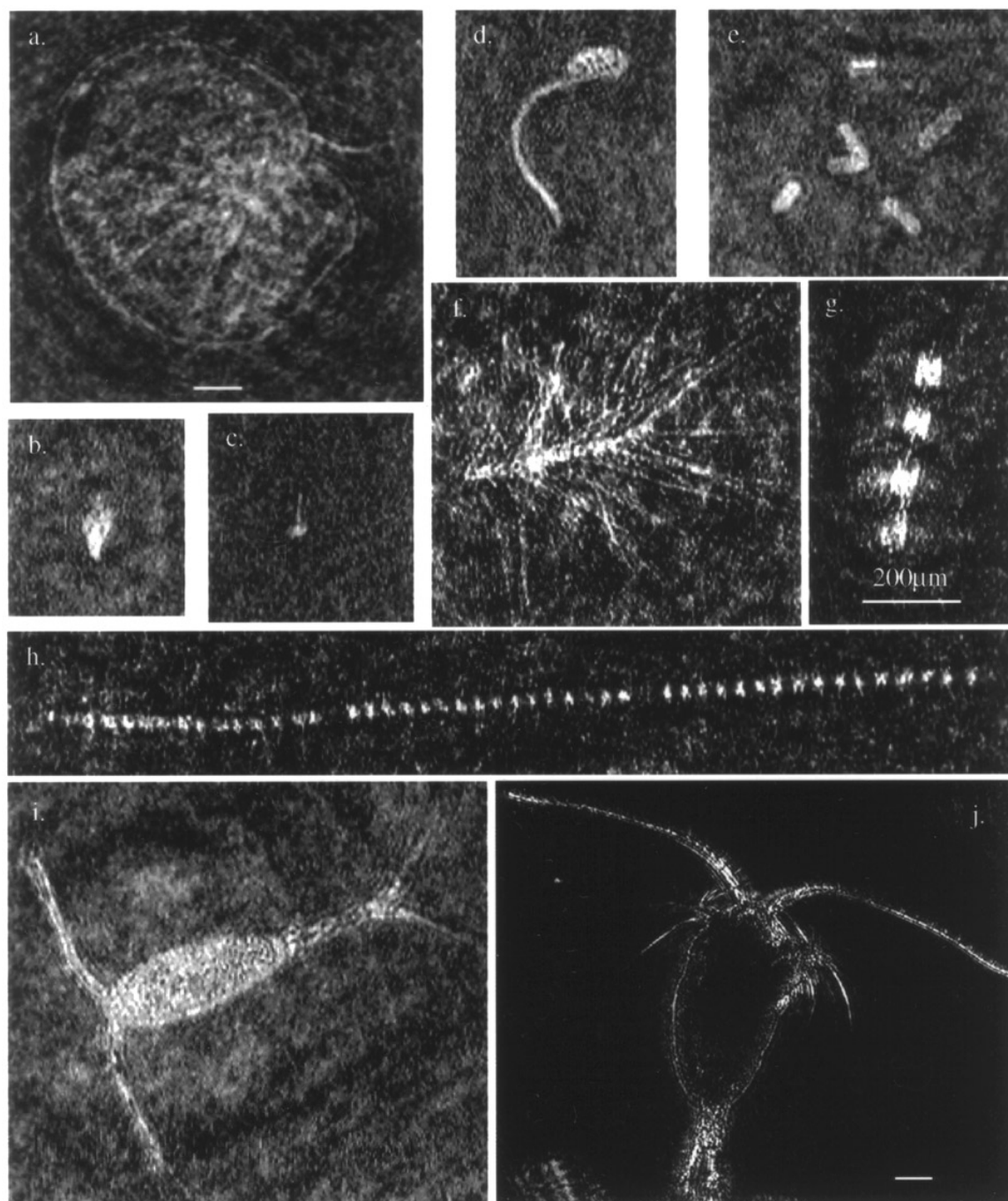


Figure 4. Plankton from Georgia Strait, BC, and classification scheme. (a) *Notiluca scintillans* (C2 class); (b), (c) dinoflagellates (C1 class); (d) larvacean; (e) fecal pellet cluster (FP class); (f) *Chaetoceros* (L3 class); (g) *Ditylum* (L2 class); (h) *Thalassiosira* (L2 class); (i) copepod; (j) copepod from laboratory using off-axis system. Scale shown in (g). (a) and (j) are at $\frac{1}{2}$ and $\frac{1}{3}$ magnification to the rest.

concentration, the operator's ability to classify particles and the desired accuracy of focusing.

The analysis procedure can be greatly accelerated by employing automated object detection, as scanning for in-focus particle images is by far the most time consuming operation. A possible method to achieve accelerated processing is to identify the pixels of a nearly focused object as being connected and distinct from background noise, a common image processing routine known as 'blob analysis'. This tool can be used to identify a region of interest in the

volume, which can then be scanned in greater detail. As illustrated in figure 5, the focus plane can be determined from the axial (depth) intensity distribution of the particle image by finding the location of peak intensity. However, this process requires acquisition of data in many, closely spaced axial planes. There is no need to store this data—only the focused image is stored.

Since background speckle noise and fringes found in in-line recorded images (e.g. figure 4(i)), are major limiting factors for automatic focusing, off-axis holography,

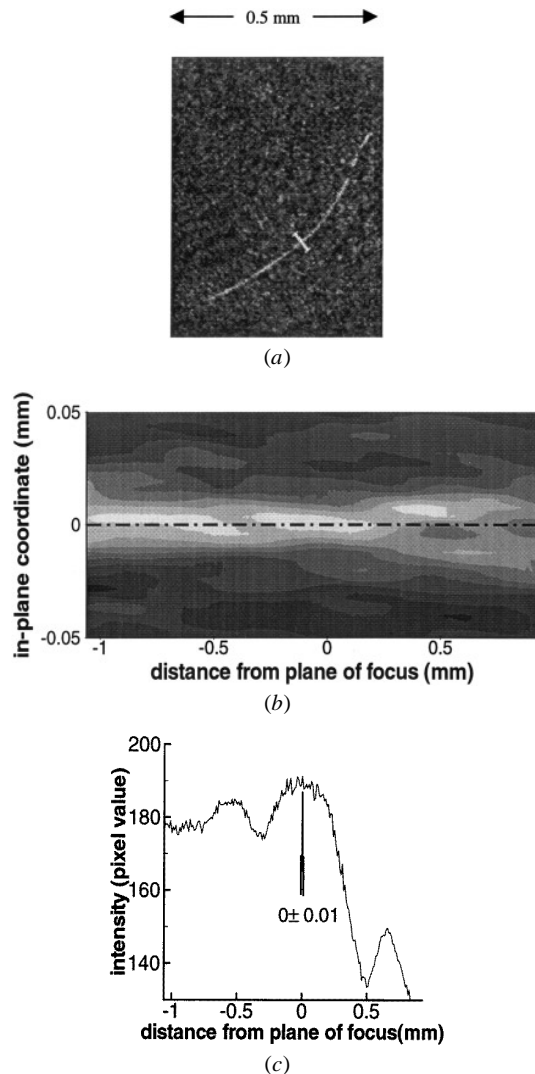


Figure 5. (a) Reconstructed image of *Skeletonema*; (b) intensity variations in a plane containing the line shown in (a) and a line perpendicular to the plane in (a). Map created from a series of images sequentially recorded while scanning in depth; (c) intensity distribution along the dashed centreline in (b).

such as described by Zhang *et al* (1997) offers significant advantages. It provides substantial improvement in the signal-to-noise ratio and substantially reduces the fringes (caused, for example, by out-of-plane objects) in the reconstructed volume. An example of a copepod (figure 4(j)) recorded in the laboratory with this off-axis system clearly shows the extent of reduction in noise. Recording off-axis holograms with the submersible holocamera requires the relatively simple modification of splitting the laser output to provide a reference beam, which is separated from the subject beam (which illuminates the sample volume). It obviously needs an additional enclosed path to the film. In ocean applications where the particle concentration varies substantially, having an undisturbed reference beam is a major advantage. Consequently, we plan to modify the current system to off-axis holography.

3. Results

3.1. Deployment tests

The current paper presents results from our two latest deployments. Deployment A results are derived from holograms taken at midday on September 2, 1996 in East Sound, a fjord in the Orca Islands found in the southern region of Georgia Strait. Results from Deployment B are derived from a 15 min vertical scan taken at midday, mid-September 1998 in Georgia Strait, British Columbia. The water in these regions tends to be relatively clear, i.e. it is dominated by resolvable particles, as opposed to water with a high concentration of particles below our resolution limit, which just destroy the coherence of the laser beam as it passes through the sample volume.

3.2. Particle characteristics

Samples of the more commonly encountered particles found in the aforementioned holograms are shown in figure 4. Except for the *Noctiluca* in figure 4(a) and the copepod in figure 4(j) they are all from deployment B. During analysis we categorize the particles based on readily observed geometric characteristics. Each classification group is associated with an arbitrarily assigned label (C for circular and L for linear). Phytoplankton examples shown include: diatom chains having clearly distinguished cells and no setae (L2), such as *Ditylum* (figure 4(g)) and *Thalassiosira* (figure 4(h)), diatoms with setae (L3), such as *Chaetoceros* (figure 4(f)), dinoflagellates smaller than $120\ \mu\text{m}$ (C1), samples of which are shown in figures 4(b) and (c) and dinoflagellates larger than $120\ \mu\text{m}$ (C2) such as the *Noctiluca* (figure 4(a)). Other examples of phytoplankton (from deployment A and earlier) can be found in Katz (1999). Examples of zooplankton include copepods (figures 4(i) and (j)) and a small larvacean (figure 4(d)), which are both conspicuous in the food web. The copepod is a major grazer and a predominant food source for many fish. The larvacean indirectly provides marine snow to feeders in lower reaches by periodically casting off a mucus house that accumulates plankton and other debris as it drifts downward. Figure 4(e) shows a cluster of what are apparently fecal pellets from zooplankton (A Alldredge, private communication) designed as FP in the later figures. Based on examination of figure 4(e), Alldredge believes that the producers may be larvaceans, krill or copepods. From the size of the pellets and the absence of mucus houses surrounding them, it seems unlikely that they are generated by larvaceans. Furthermore, although this particular example shows what appears to be a V-shaped pellet, typical of krill (A Alldredge, private communication), no krill have been observed in the holograms. Also, the V shape has not been observed elsewhere in this or other holograms, suggesting that the image shown is probably a consequence of overlapping pellets. Copepods on the other hand, were observed in the same sample volumes and have the correct size ($745 \pm 3\ \mu\text{m}$ length, $278 \pm 39\ \mu\text{m}$ diameter) relative to the fecal pellets ($125 \pm 22\ \mu\text{m}$ length, $51 \pm 6\ \mu\text{m}$ diameter) to be the producers.

The species distributed from three holograms recorded at different depths in deployment A are shown in figure 6 and

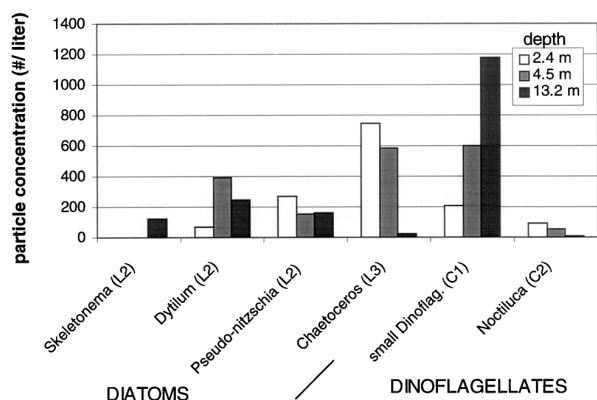


Figure 6. Plankton class distributions observed in holograms recorded at three different depths during deployment A.

their respective length distributions are presented in figure 7. They are derived from scans of approximately 20% of each reconstructed volume. The species distribution shows that *Chaetoceros* (L3) and *Noctiluca* (C2) are concentrated in the upper regions. The large average length ($1588 \pm 674 \mu\text{m}$) of L3 and diameter ($566 \pm 135 \mu\text{m}$) of C2 skew the size distribution, which otherwise is dominated by C1, the small dinoflagellates ($85 \pm 33 \mu\text{m}$). Also noticeable is that the diatom *Skeletonema* ($702 \pm 352 \mu\text{m}$) are only present at the deepest sample (13.2 m). We also found that the *Ditylum* species are markedly shorter at 13.2 m ($487 \pm 274 \mu\text{m}$) compared with their length at 4.5 m ($1453 \pm 640 \mu\text{m}$), with $p < 0.01$, the probability that this difference is just a random fluctuation between samples of one population, assuming normal size distributions. The shorter average length is perhaps due to subdued growth rates associated with reduced photosynthesis at this depth or the influence of localized turbulence in breaking diatom chains (Rines 1998). Also, probably due to local turbulence, none of the diatom classes show directional preference in any of these regions, unlike what has been stated in Katz (1999). Note that when the orientation of particles in three dimensions is random, 71% of the particles appear at an angle with an optical axis that is larger than 45° (the percentage of a sphere's surface area within that solid angle). Thus, it is not unexpected that most of the plankton in the reconstructed volume appear in planar view, close to being perpendicular to the optical axis of the hologram. The lengths for linear species given above are projections normal to the optical axis and therefore are shorter than the actual lengths. Because we do have the depth information, it is possible to focus on the extremities of the organism and thus measure its full length. However, we have not yet completely implemented such a routine.

There is an apparent discrepancy in particle concentration between figures 6 and 7. This difference is a result of figure 6 presenting only particles that have been categorized with a high degree of confidence, which is as low as 40% in the holograms of deployment A. This low yield is partially caused by delayed classification of saved image files, which was initially done after all the images were acquired. Consequently, while analysing data from deployment B, we modified the analysis procedure and categorized the particles while scanning the reconstructed volumes. The latter allows

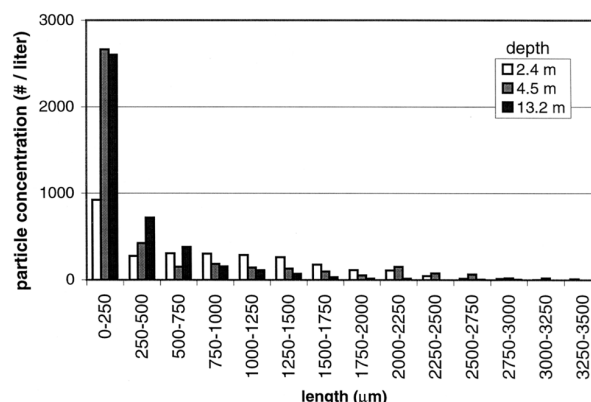


Figure 7. Size distributions of the plankton at three different depths during deployment A.

focusing in different nearby planes, a process that improves our ability to make classification decisions. Holograms from deployment B also have significantly less background noise compared with those of deployment A (perhaps because there are less submicron particles in the sample), which helps with identifying features for classification purposes.

During deployment B, we made a vertical transect of the water column, moving continuously upward at a rate of 2 m min^{-1} (16 cm s^{-1}). Data from our pumped CTD (figure 8) show two thermoclines/pycnoclines at depths of 8 and 14 m. Considering that the independently measured salinity, temperature, oxygen content and light transmissivity (also shown in figure 8) change abruptly at the same elevation, the data indicates that regions I and II contain two masses of water that have different origins. The differences in particle concentrations (obtained from analysed holograms) support this claim as well. The upper layer, which extends between the surface down to a depth of 6 m (region I in figure 8), seems to be well mixed. This conclusion is based on the fact that all the distributions, including the particles, are quite uniform. Conversely, there are considerable gradients in concentration of O_2 , light transmission and particle distributions in the region located between the two pycnoclines (region II). Thus, the data indicate that region II is not well mixed.

The percent saturation of dissolved oxygen is 100% in region I, and it decreases from 95% to 90% in region II. Between them there is a thin layer of supersaturated water. With respect to these measurements it is worth mentioning that the wind speed was low (less than 5 knots), it was sunny, and the scan occurred at 12.30 pm. Supersaturation in this instance may occur due to upward movement of the pycnocline and/or the relatively high midday oxygen production from photosynthesizing phytoplankton. The ability of a thin layer to maintain a concentration that is higher than the surrounding flow depends on the local turbulence level. In the absence of turbulent mixing, the mass diffusion is reduced to molecular levels. Being situated on a pycnocline with poorly mixed flow below suggests that the turbulence in this supersaturated layer is stabilized by the local density gradients. Such phenomena, with even significantly higher levels of supersaturation, have been previously observed. For example, a high degree of methane supersaturation confined to the pycnocline has been revealed from vertical

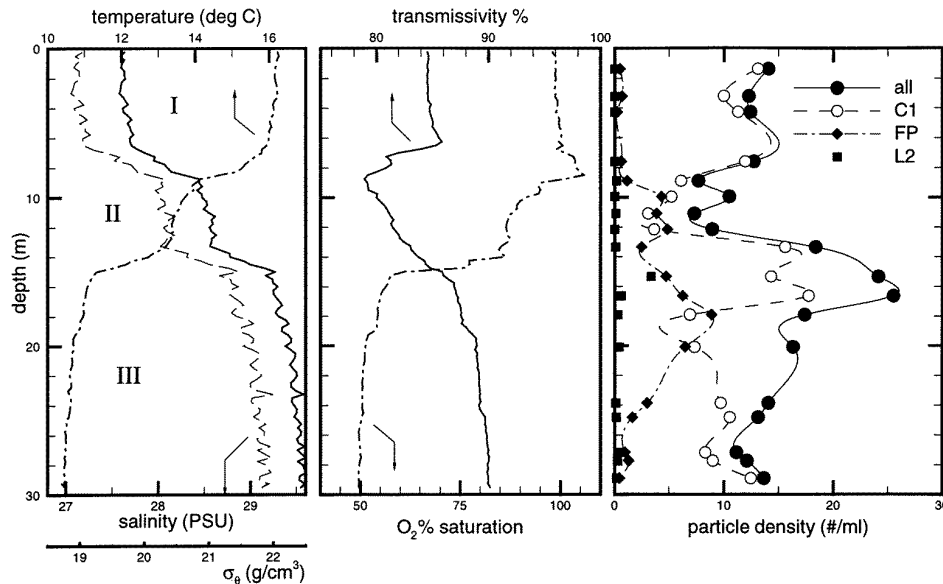


Figure 8. CTD scan and particle density characteristics obtained from the submersible holocamera during a 15 min scan of the water column.

transects off the California coast (Cynar and Yayanos 1992). Similarly, plankton blooms have led to a high degree of oxygen supersaturation in some instances (Kaas *et al* 1991, Yacobi *et al* 1993, Cloern 1996). Vertical transects from Kass *et al* show maxima in dissolved oxygen content (as high as 150% saturation) in the region of the pycnocline near fluorescence peaks marking high concentration of plankton. Surprisingly, a maximum in phytoplankton concentration, usually found at pycnoclines (Condie 1998), was not detected here, at least not within our resolution range. However, the light transmissivity (% attenuation of 660 nm beam over a 250 mm depth) shows a drop from 86% to 79% during transition from region I to region II, in spite of the overall drop in resolved particle concentration. The most likely cause of this trend is increased abundance of submicron particles, which are too small to be detected in holograms and thus are unaccounted for in concentration profiles. The 7% change in light transmission is apparently not enough to reduce the quality of our holograms significantly. In contrast, the strong refractive index fluctuations in the lower thermocline (14 m) destroyed the coherence of the reference beam, making it impossible to reconstruct the hologram recorded at that level. As noted before, this problem can be eliminated by using an off-axis reference beam that does not pass through the water.

The particle concentrations are determined by analysing at least 20 cm³ from each of 17 reconstructed images out of the 25 holograms recorded during the transect. Concentrations in the lower thermocline are based on an analysis of 40 cm³. Even though the latter is less than 6% of the recorded sample volume, it is apparently sufficient to perform statistical analyses, since each of the samples contains approximately 900 particles. The majority of the particles are small dinoflagellates (C1) and fecal pellet clusters (FP) which, as noted before, we attribute to copepods.

Zonal differences in particle concentrations support the notion that regions I and II have different origins. Not only is there a difference in the overall particle concentrations,

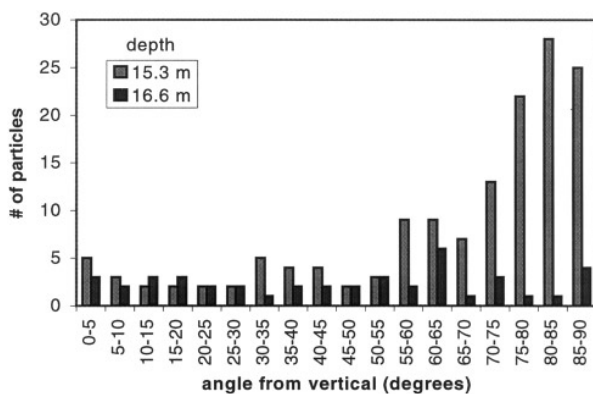
but there is also a considerable difference in composition. Ratios of C1 to FP are 1:1 in region II and 18:1 in region I. The maximum overall particle concentration is centred about the lower pycnocline, where there are peak concentrations of small dinoflagellates (C1). There is also a peak concentration of assorted diatom chains (L2), mostly *Thalassiosira* (figure 4(h)) with average length of $717 \pm 440 \mu\text{m}$ at the lower edge of this lower pycnocline. The existence of chlorophyll maxima at pycnoclines (indicating high concentrations of phytoplankton) is apparently fairly common (Steele and Yentsch 1960, Strickland 1968, Le Febre 1986), although the reasons for this are not completely understood. One possible cause is the previously mentioned stability of such regions to vertical perturbations, which may also inhibit turbulence (Condie 1998). Supporting evidence of reduced turbulence at this depth is provided by the orientation of the diatoms shown in figure 9. At this depth (15.3 m) the majority of diatoms, irrespective of size, are almost horizontal, while just 1 m below this location there is no directional preference. The latter would occur if turbulence dominates over the viscous settling mode of a particle.

In deeper regions, just below the observed diatom and dinoflagellate concentration peaks there is a maximum in FP concentration. The overabundance of fecal pellets to their producers, which only numbered one or two in a 40 ml volume (16 m) at the time of the scan, is indicative of a migration from this region—a well known behaviour of copepods and other zooplankton (Frank and Widder 1999). Zooplankton make diel migrations to forage at night in the photic zone and tend to spend the day in deeper, darker regions. This strategy apparently protects them from being eaten by predators (fish) that rely on vision to detect their prey (Zaret and Suffern 1976). The present peak in pellets concentration, found directly below the peak in dinoflagellate concentration, is similar to the night-time distribution of copepods reported in Tiselius (1998), where a maximum

Table 1. Nearest-neighbour distances from field data compared with random distributions.

Location	Depth (m)	Classification	Quantity (N)	Average nearest-neighbour distance (mm)		z-score ^a
				Field sample	Random	
Deployment B	13.3	ALL	439	1.72 ± 1.20	2.21 ± 0.87	−11.8
		C1	370	1.83 ± 1.28	2.35 ± 0.94	−10.7
		FP	59	4.27 ± 2.06	4.60 ± 1.92	−1.3
	15.3	ALL	652	1.55 ± 1.06	1.92 ± 0.76	−12.4
		C1	394	1.87 ± 1.25	2.28 ± 0.90	−9.2
		L	102	3.71 ± 1.76	3.75 ± 1.54	−0.3
	16.6	FP	128	3.08 ± 1.72	3.45 ± 1.43	−2.9
		ALL	606	1.64 ± 1.03	1.96 ± 0.76	−10.4
		C1	431	1.92 ± 1.12	2.22 ± 0.88	−7.3
		L	28	5.14 ± 2.60	6.08 ± 2.59	−1.9
		FP	137	3.09 ± 1.68	3.33 ± 1.35	−2.1
Deployment A	2.4	ALL	693	3.79 ± 1.82	4.22 ± 1.62	−7.0
		C1	87	8.46 ± 4.65	8.68 ± 3.55	−0.6
		Noctiluca	34	10.34 ± 8.15	12.33 ± 5.26	−2.2
		L	414	4.38 ± 2.24	5.02 ± 1.97	−6.7
		Chaetoceros	163	6.24 ± 3.25	7.00 ± 2.82	−3.4
		Pseudo-nitzschia	58	7.80 ± 6.25	10.13 ± 4.15	−4.3
		Dytilum	25	9.73 ± 7.67	13.97 ± 5.89	−3.6
		ALL	252	3.34 ± 1.79	3.69 ± 1.46	−3.8
	4.5	C1	30	6.49 ± 4.56	8.41 ± 3.91	−2.7
		L	136	4.68 ± 2.25	4.62 ± 1.87	0.4
		Chaetoceros	29	8.34 ± 4.50	8.53 ± 3.91	−0.3
		Dytilum	25	9.88 ± 2.90	9.01 ± 4.14	1.0
	13.2	ALL	583	3.16 ± 1.59	3.60 ± 1.42	−7.5
		C1	187	4.78 ± 2.17	5.36 ± 2.16	−3.7
		L	338	3.84 ± 1.98	4.33 ± 1.73	−5.2
		Pseudo-nitzschia	24	7.66 ± 6.04	11.85 ± 5.28	−3.9
		Dytilum	39	7.58 ± 6.56	9.65 ± 4.17	−3.1

^a $z - \text{score} = \frac{\bar{x}_{\text{sample}} - \bar{x}_{\text{random}}}{\sigma_{\text{random}} / \sqrt{N}}$. The difference is statistically significant when $|z - \text{score}| > 2$, ($p < 0.05$).

**Figure 9.** Orientation of diatoms (L2, L3) near the lower pycnocline of deployment B.

copepod concentration is found directly below a peak in chlorophyll-induced fluorescence.

3.3. Nearest-neighbour distances

We calculate the nearest-neighbour distances between particles identified in the holograms recorded at and near a depth of 15.3 m (location of peak concentration of diatoms). The results are compared with the ensemble-averaged nearest-neighbour distance that would be obtained in a random distribution. The qualitative difference between the physical data and a random distribution is readily apparent

from figure 10. The quantitative differences, summarized in table 1, show field data and random mean values as well as the z-score of each difference. Sample data that have z-scores with absolute values greater than 2.0 are significantly different from the random distributions (Freedman *et al* 1980). In other words, the probability that such a difference is merely a random fluctuation of a sample mean from the random population is less than 5% ($p < 0.05$). The results clearly show that at all depths the mean interparticle distance is substantially smaller ($p < 0.001$) than the mean random distance. Within each class, clustering is most significant for the small dinoflagellates (C1) and least significant for the fecal pellets (FP) and diatoms (L). Interestingly, the diatoms do not cluster at 15.3 m, where their concentration peaks and their uniform orientation (figure 9) suggest that the environment is relatively quiescent.

Data from the holograms of deployment A also show general clustering between particles ($p < 0.001$) at all depths, but the trend is least significant at 4.5 m. Here the diatoms (L) as well as its subclasses of Chaetoceros and Dytilum appear to be randomly distributed. The small dinoflagellates (C1) are also randomly distributed at 2.4 m, in sharp contrast to all the other classes at that depth, and unlike what is observed in deployment B.

4. Summary

This paper demonstrates that the submersible holocamera is capable of recording the spatial distribution of particles

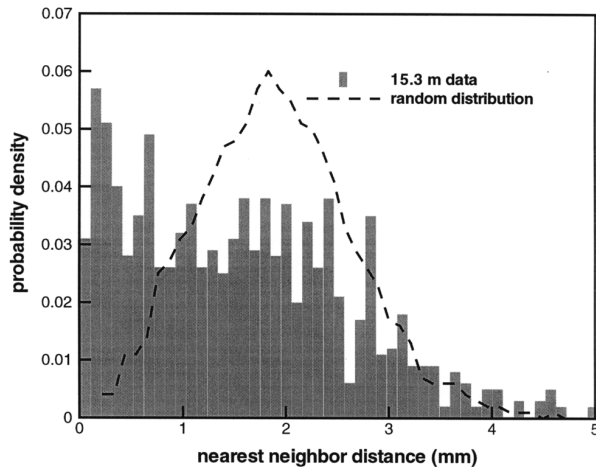


Figure 10. Measured nearest-neighbour distances and expected values from a random distribution.

over a comparatively large sample volume (732 ml). The resolution is about $3\ \mu\text{m}$ for linear objects and $10\text{--}20\ \mu\text{m}$ for spherical objects, at least through the forward half of this volume. Although only small fractions of the holograms from two deployments have been analysed up to this point, a substantial amount of information can be gleaned from them. The results include particle concentrations and classifications along with class characteristics such as mean size, orientation and nearest-neighbour distances. Onboard CTD, O_2 concentration and light transmission data gathered simultaneously provide the context for the holographic results, and thus make it possible to arrive at some conclusions concerning plankton dynamics (and its relationship to the local flow structure) in the ocean. For example, from a 15 min vertical scan of the water column, we find striking variations in class-dependent particle concentrations, sizes and orientations. Included are maxima about a pycnocline and just below it, corresponding to increased dinoflagellate/diatom population and fecal pellets. These trends can be associated with zooplankton migration. We have also found that the diatoms in the region of peak concentration, at the lower edge of a pycnocline, show strong tendencies toward horizontal orientation, perhaps indicative of the role that reduced turbulence plays in the formation of thin layers. There is also clear evidence of clustering at almost all depths.

The analysis procedures are still in the process of being automated to facilitate processing of the enormous amount of data that is contained in the holograms. Conversion of our system to off-axis holography to further improve the quality of our images (based on our laboratory experience) is also planned. In the future, we also plan to measure the instantaneous three-dimensional velocity distributions within the oceanic sample volumes, which would provide direct information on the local structure of turbulence, shear stresses, etc. The process would involve recording of double-exposure holograms and implementation of holographic particle image velocimetry tools (Zhang *et al* 1997) that have already been developed in our laboratory.

Acknowledgments

This development of the holocamera was sponsored by the National Science Foundation, Oceanographic Technology Program managed by Larry Clark, under grant OCE-9107564. Funding for deployment B and further development of analysis procedures was provided by the Office of Naval Research, managed by Sharon Beermann-Curtin under N00014-97-1-0281. The authors would also like to thank Jennifer Abras for her assistance in scanning the reconstructed volumes. We are also grateful to Tom Osborn for useful discussions and his review of the manuscript and to Jan Rines and Alice Alldredge for their assistance in identifying the particles.

References

- Barnhart D H, Adrian R J and Pappen G C 1994 Phase conjugate holographic system for high resolution particle image velocimetry *Appl. Opt.* **33** 7159–70
- Buskey E J, Baker K S, Smith R C and Swift E 1989 Photosensitivity of the oceanic copepods *Pleuromamma gracilis* and *Pleuromamma xiphias* and its relationship to light penetration and daytime depth distribution *Mar. Ecol. Prog. Ser.* **55** 207–16
- Carder K L 1979 Holographic microvelocimeter for use in studying ocean particle dynamics *Opt. Eng.* **18** 524–5
- Cloern J E 1996 Phytoplankton bloom dynamics in coastal ecosystems: a review with some general lessons from sustained investigation of San Francisco Bay, California *Rev. Geophys.* **34** 127–68
- Collier R, Burkhardt C and Lin L 1971 *Optical Holography* (New York: Academic)
- Condie S A 1999 Settling regimes for non-motile particles in stratified waters *Deep-Sea Res.* **I** **46** 681–99
- Cynar F J and Yayanos A 1992 The distribution of methane in the upper waters of the Southern California Bight *J. Geophys. Res.* **97** 11 269–85
- Forward R B 1988 Diel vertical migration: Zooplankton photobiology and behaviour *Oceanography and Marine Biology—An Annual Review* **26** 361–93
- Foster E and Watson J 1997 Holography for underwater inspection and measurement: an overview of current work *Opt. Laser Technol.* **29** 17–23
- Frank T M and Widder E A 1999 The correlation of downwelling irradiance and staggered vertical migration patterns of zooplankton in Wilkinson Basin, Gulf of Maine *J. Plank. Res.* at press
- Freedman D, Pisani R and Turves R 1980 *Statistics* (New York: W W Norton and Co)
- Gallager M, Davis C S, Epstein A W, Solow A and Beardsley R C 1996 High resolution observations of plankton spatial distributions correlated with hydrography in the Great South Channel, Georges Bank *Deep-Sea Res.* **II** **43** 1627–63
- Heflinger L O, Stewart G L and Booth C R 1978 Holographic motion pictures of microscopic plankton *Appl. Opt.* **17** 951–4
- Hobson P R, Krantz E P, Lampitt R S, Rogerson A and Watson J 1997 A preliminary study of the distribution of plankton using hologrammetry *Opt. Laser Technol.* **29** 25–33
- Karp-Boss L, Boss E and Jumars P A 1997 Nutrient fluxes to planktonic osmotrophs in the presence of fluid motion *Oceanogr. Mar. Biol. Ann. Rev.* **34** 71–107
- Kass H, Larsen J, Mohlenberg F and Richardson K 1991 The *Chrysochromulina polyylepis* bloom in the Kattegat (Scandinavia) May–June 1988. Distribution, primary production and nutrient dynamics in the late stage of the bloom *Mar. Ecol. Prog. Ser.* **79** 151–61
- Katz J, Donaghay P L, Zhang J, King S and Russell K 1999 Submersible holocamera for detection of particle

- characteristics and motions in the ocean *Deep-Sea Res.* **I 46** 1455–81
- Katz J, O'Hern T J and Acosta A J 1984 An underwater holographic camera system for detection of microparticulates *Proc. ASME Cavitation and Multiphase Flow Forum* (New Orleans, LA)
- Kiorboe T 1997 Small-scale turbulence, marine snow formation and plantivorous feeding *Sci. Mar.* **61** 141–58
- Knox C 1966 Holographic microscopy as a technique for recording dynamic microscopic subjects *Science* **153** 989–90
- Knox C and Brooks R E 1969 *Proc. R. Soc. B* **174** 115
- Le Fevre J 1986 Aspects of the biology of frontal systems *Adv. Mar. Biol.* **23** 163–299
- Marrase C, Saiz E and Redondo J (ed) 1997 *Lectures on Plankton and Turbulence* (*Scientia Marina* vol 61) International Centre for Coastal Resources Research (Barcelona), p 238
- Meng H and Hussain F 1995 In-line recording and off-axis viewing technique for holographic particle velocimetry *Appl. Opt.* **34** 1827–40
- O'Hern T J, D'Agostino L and Acosta A J 1988 Comparison of holographic and Coulter counter measurements of cavitation nuclei in the ocean *J. Fluids Eng.* **110** 200–7
- Rothschild B J and Osborn T R 1988 Small-scale turbulence and plankton contact rates *J. Plank. Res.* **10** 465–74
- Rines J and Donaghay P 1998 Interactions of small-scale physical mixing processes with the structural morphology and bloom dynamics of non-spheroid diatoms *ONR Annual Report*
- Steele J H and Yentsch C S 1960 The vertical distribution of chlorophyll *J. Mar. Biol. Assoc.* **39** 217–26
- Strickland J D H 1968 A comparison of profiles of nutrient and chlorophyll concentration taken from discrete depths and by continuous recording *Limnol. Oceanogr.* **13** 388–91
- Stewart G L, Beers J R and Knox C 1973 Application of holographic techniques to the study of marine plankton in the field and in the laboratory *Developments in Laser Technology-II, Proc. Soc. Photo-Opt. Instrum. Eng.* (San Diego, CA) vol 41, p 193
- Svendsen H 1997 Physical oceanography and marine ecosystems: some illustrative examples *Sci. Mar.* **61** 93–108
- Tao B, Katz J and Meneveau C 1991 Application of HPIV data of turbulent duct flow for turbulence modelling *Proc. 3rd ASME/JSME Joint Fluids Engineering Conf. (July 1999, San Francisco, CA)* (New York: ASME) paper FEDSM99-7281
- Tiselius P 1998 An *in situ* video camera for plankton studies: design and preliminary observations *Mar. Ecol. Prog. Series* **64** 293–9
- Vikram C S 1992 *Particle Field Holography* (Cambridge: Cambridge University Press)
- Watson J, Hobson P R, Krantz E, Lampitt R S and Rogerson A 1995 *Proc. SPIE* **2577** 191–9
- Yacobi Y Z, Kalikhman I, Gophen M and Walline P 1993 The spatial distribution of temperature oxygen, plankton and fish determined simultaneously in Lake Kinneret, Israel *J. Plank. Res.* **15** 589–601
- Zaret T M and Suffern J S 1976 Vertical migration in zooplankton as a predator avoidance mechanism *Limnol. Oceanogr.* **21** 804–13
- Zhang J, Tao B and Katz J 1997 Turbulent flow measurement in a square duct with hybrid holographic PIV *Exp. Fluids* **23** 373–81